Digital Image Processing for the Quantification of Pneumonic Area in the Lungs of Chronically Lead-Exposed Wistar Albino Rats in an Intergenerational Model

Procesamiento digital de imágenes para la cuantificación de áreas neumónicas en pulmones crónicamente expuestos a plomo en ratas Wistar en un modelo intergeneracional.

Rivera-Rojas, Gerardo N[1], Galván-Tejada, Carlos E[2]*, González-Curiel Irma E[3], Acosta-Cruz, Erika[4].

ABSTRACT

The evaluation of lung tissue can be done by several approaches. While structural integrity is critical for accurate diagnosis of different pathologies, scientific research uses specific tools to facilitate evaluation based on the characteristics of the study, the needs of the researcher, and available resources. Most software tools lack versatility and are perceived as black boxes, requiring extensive knowledge of the subject and software functionality to fully utilize their capabilities. Additionally, these specialized tools, often from the private sector, are costly and require specific inputs. Thus, conducting quantitative analysis of morphological features in a qualitative manner requires substantial expertise or extensive training time to ensure accurate evaluations. Therefore, the proposed software for alveolar area quantification, developed using histological images of lung tissue stained with hematoxylin-eosin, aims to provide a user-friendly interface for the end user, enabling quick and simple analyses that can be executed on devices with limited resources. The images were obtained from different groups exposed to different concentrations of lead (5, 10, 15 mg/kg) administered intraperitoneally. This approach seeks to bridge the gap between the need for precise structural analysis and the accessibility of effective tools, enhancing the efficiency and accuracy of lung tissue evaluation in research requirements.

Keywords: Chronic Lead Exposure, Digital image processing, segmentation and pulmonary fibrosis

https://doi.org/10.25009/rmuv.2025.1.130

Recibido: 07/03/25
Aprobado: 29/04/25

[1]Licenciatura, Maestría en ciencias del procesamiento de la información, Universidad autónoma de zacatecas, Zacatecas, México.
[2]Doctorado, Centro de Investigación e Innovación en Biomédica e Informática, Universidad Autónoma de Zacatecas, Zacatecas, México.
*Autor de Correspondencia: ericgalvan@uaz.edu.mx 492 544 0968
[3]Doctorado, Laboratorio de inmunotoxicología y terapéutica experimental, Universidad Autónoma de Zacatecas, Zacatecas, México.
[4]Doctorado, Departamento de Biotecnología., Universidad Autónoma de Coahuila, Saltillo, Coahuila, México

RESUMEN

La evaluación del tejido pulmonar puede abordarse de diversas maneras. Si bien la integridad estructural es fundamental para un diagnóstico preciso de diferentes patologías, la investigación científica requiere herramientas específicas que faciliten la evaluación según las características del estudio, las necesidades del investigador y los recursos disponibles. La mayoría de las herramientas de software carecen de versatilidad y son percibidas como "cajas negras", ya que exigen un conocimiento extenso tanto del tema como del funcionamiento del software para aprovechar completamente sus capacidades. Además, estas herramientas especializadas, a menudo provenientes del sector privado, son costosas y requieren insumos específicos. Por todo esto, realizar análisis cuantitativos de características morfológicas de manera cualitativa requiere una experiencia considerable o un tiempo extenso de capacitación para garantizar evaluaciones precisas. Por lo tanto, el software propuesto para la cuantificación del área alveolar, desarrollado utilizando imágenes histológicas de tejido pulmonar teñidas con hematoxilina-eosina, tiene como objetivo proporcionar una interfaz fácil de usar para el usuario final, permitiendo análisis rápidos y simples que pueden ejecutarse en dispositivos con recursos limitados. Las imágenes fueron obtenidas de diferentes grupos expuestos a diversas concentraciones de plomo (5, 10, 15 mg/kg) administradas por vía intraperitoneal. Este enfoque busca cerrar la brecha entre la necesidad de análisis estructurales precisos y la accesibilidad a herramientas efectivas, mejorando la eficiencia y precisión de la evaluación del tejido pulmonar en los contextos de investigación.

Palabras clave: Exposición crónica a plomo, Fibrosis pulmonar, Procesamiento digital de imagen y Segmentación.

INTRODUCTION

Lead (Pb) is a significant anthropogenic toxic pollutant historically utilized in products such as gasoline, household goods, toys, paints, and ceramics (Hoover et al., 2023). Its extensive use was largely due to its favorable properties, including durability, malleability, and resistance to corrosion. However, the severe health consequences associated with Pb exposure prompted regulatory actions to restrict its use starting in the late 1970s. These restrictions have reduced exposure in some populations, yet Pb remains a global critical public health concern. This is largely attributed to its persistence in the environment and its ability to exert toxic effects even at low exposure levels (Charkiewicz & Backstrand, 2020).

One of the unique and concerning characteristics of Pb is its capacity to bioaccumulate within the human body. Unlike many other contaminants that are metabolized and excreted, Pb is predominantly stored in bones, where 90–95% of the body's Pb burden is sequestered. This bone-bound Pb can be gradually released into the bloodstream over time, especially during periods of increased bone turnover such as pregnancy, lactation, or aging, thereby maintaining elevated blood Pb levels long after external exposure has ceased (Yu et al., 2023)

Geochemically, Pb is the second most toxic metal after arsenic (As) and constitutes approximately 0.002% of Earth’s crust (Tarragó & Brown, 2017). Human exposure to Pb occurs primarily through environmental and occupational pathways. Key sources include Pb salts and oxides present in atmospheric dust, emissions from automobile exhausts, residues in old paints, and contamination of food and water supplies (Kumar et al., 2020). These pathways highlight the widespread nature of Pb contamination, affecting populations across diverse regions and socioeconomic statuses.

The health impacts of Pb exposure are both acute and chronic, affecting multiple organ systems. Chronic exposure is particularly concerning as it has been strongly associated with a range of long-term health issues. For instance, it can impair cognitive function, leading to developmental delays and reduced IQ in children (X. Wang et al., 2018a). It also contributes to cardiovascular diseases, such as hypertension and heart disease, and is a known carcinogen linked to respiratory neoplasms, particularly in lung tissue (Ding et al., 2023). Elevated blood Pb levels during early development can disrupt postnatal growth (Jiang et al., 2022), deregulate the neuroendocrine system (Dos Santos et al., 2022), and impair auditory function, reducing hearing capacity in infants and children (Xu et al., 2020).

In adults, Pb exposure poses serious risks to the central nervous system, leading to neurological disorders, and can also impair renal function, contributing to chronic kidney disease (Kothapalli, 2021); (Jing et al., 2020). Furthermore, Pb exposure during pregnancy is particularly detrimental. Maternal Pb can cross the placental barrier, adversely affecting fetal development and growth, particularly during the early stages of gestation (X. Wang et al., 2018b). These wide-ranging and persistent effects underscore the critical need for ongoing efforts to mitigate Pb exposure and address its public health implications. Some approaches for determining morphological damage through pixel counting within texture ranges have been implemented with excellent results (D. Wang et al., 2020).

Oxidative stress plays a critical role in cellular damage, particularly following exposure to heavy metals such as lead (Pb). This stress disrupts macromolecules, including lipids, proteins, and DNA, triggering pathways involved in cell survival and programmed cell death. Pb exposure has been linked to neurological disorders, developmental abnormalities, and cardiovascular diseases due to its ability to generate reactive oxygen species (ROS) that overwhelm antioxidant defenses, leading to sustained molecular damage (Paithankar et al., 2021).

Key signaling pathways mediate cellular responses to Pb-induced oxidative stress. The NF-κB pathway modulates inflammation (L. Wang et al., 2021). While the NRF2 pathway regulates antioxidant defenses Pb exposure also affects the JAK-STAT pathway, which influences immune function and apoptosis (Li et al., 2023). and the JNK pathway, which is associated with stress-induced cell death (Fang et al., 2021). Additionally, Pb induces hypoxia-like responses via the HIF pathway (Aschner et al., 2023).Together, these pathways form a complex network, highlighting the multifaceted nature of cellular responses to oxidative stress and environmental insults like heavy metal exposure.

Lead (Pb) exposure has been shown to induce significant histopathological alterations in various organs, including the liver and lungs. While studies have extensively documented Pb-induced hepatic damage—ranging from vascular disruption to necrosis (Kou et al., 2020), the pulmonary effects of Pb exposure remain a critical area of investigation. The lungs, as a primary interface for gas exchange, are highly susceptible to oxidative stress and inflammatory responses triggered by Pb accumulation. Such exposure may lead to vascular congestion, alveolar damage, and pneumonic lesions, ultimately compromising respiratory function.

Histological analysis of lung tissue provides a crucial tool for identifying structural alterations associated with Pb toxicity. By quantifying pneumonic areas and assessing cellular damage, this study aims to contribute to a deeper understanding of Pb-induced pulmonary pathology, complementing findings from other organ systems and highlighting the systemic nature of heavy metal toxicity.

The lung, essential for gas exchange, depends on the integrity of its pulmonary alveolar architecture to maintain proper function. Inflammatory conditions like pneumonia, which can be persistent and fatal, significantly compromise lung performance (West et al., 2021), while limited research exists on the direct role of lead (Pb) exposure in triggering pneumonia, studies suggest that Pb disrupts immune system balance, favoring the production of pro-inflammatory cytokines that contribute to tissue damage (Dietert & Piepenbrink, 2006). Evidence from animal studies reinforces these findings. Mice exposed to Pb inhalation for six months exhibited reduced lung compliance, with pathological changes progressing from emphysema to fibrosis. Notably, their blood Pb levels mirrored those of humans occupationally exposed to heavy metals. Histological analysis further confirmed inflammation and significant collagen deposition, underscoring the profound impact of Pb on lung health (Lee & Lee, 2024).

Accurate assessment of such pathological changes often requires manual adjustments of thresholds by experienced analysts, a process that is both time-consuming and skill-dependent (Hübner et al., 2008). To address this challenge, the proposed software seeks to streamline preliminary quantitative analysis by semi-automating image processing tasks. Its primary objective is to determine potential differences in alveolar areas analyzed across experimental groups, enabling more precise comparisons. This innovative tool, described in detail below, aims to reduce the time and expertise required to obtain reliable results, making lung tissue evaluation more accessible and efficient.

MATERIALS AND METHODS

This section details the murine model used for obtaining tissue samples and photographs to observe the pulmonary area, followed by digital image processing methods for quantification.

2.1 Murine model methodology

An intergenerational murine model was generated to emulate and represent the levels of chronic lead exposure that humans may be subjected to. The project was approved by the Research Committee (COFEPRIS-19CI 32056045) and the Bioethics Committee (CEI-UAO/UAZ0002-R/2022).

Male Wistar albino rats were exposed during gestation and the first three months after weaning to different lead doses. A weekly intraperitoneal dose of $Pb(NO_3)_2$ was administered at 5, 10, and 15 mg/kg, respectively. The control group was administered a saline solution with $NaNO_3$ to rule

out any alterations induced by the nitrates themselves. All study specimens were housed in cages with *ad libitum* access to food and water in a reversed 12-hour light/dark cycle at a temperature of 25 °C until sacrifice.

2.2 Image acquisition

Rats were sacrificed by exsanguination via axillary cut. Subsequently, dissection was carried out for organ identification and extraction of the right lung, in accordance to NOM-062-ZOO-1999. After completing the histological technique and paraffin embedding, 4 µm sections of the embedded lung tissue were made and placed on albuminized slides for subsequent hematoxylin-eosin staining. The tissues were photographed using an inverted microscope, model Axio Vert A1 (Carl Zeiss) with an Olympus C-5060 Wide Zoom digital camera (5.1 megapixels).

Several photos of the slides of the lung tissue of the rats subjected to the different treatments were analyzed with software designed in collaboration with the Academic Unit of Electronic Engineering of the Autonomous University of Zacatecas.

This program can process the images to determine if there is a decrease or increase in the alveolar spaces. The software can transform the images obtained from the microscope into binarized images as shown in Figure 4, to subsequently provide pixels number values, as shown in Table 1.

2.3 Image preprocessing

The images obtained as described above were converted from Tag Image File Format (TIFF) to Joint Photographic Experts Group (JPEG) format. Subsequently, the color palette is changed to grayscale.

2.4 Image binarization

Binarization is a digital image processing technique that converts a grayscale image into a binary image with black and white pixels colors, commonly with values: 0 (black) or 1 (white). This process is important in order to segment regions of interest (ROI) and facilitates the subsequent quantification and analysis of image features.

The procedure for image binarization is described in the following steps:

1. Thresholding: After the color palette change to grayscale, a threshold value *T* is selected as cutoff point between pixels that will be classified as black or white. This value can be manually defined or automatically calculated using algorithms or given a specific task to be done.

2. Binary Value Assignment: Each pixel in the grayscale image is compared with the threshold *T*. If the pixel intensity *I* (*x*, *y*) is greater than or equal to *T*, the pixel is assigned a value of 1 (white). Otherwise, it is assigned a value of 0 (black), as is presented in equation 1.

$$B(x,y)= \{1 \text{ if } I(x,y) \geq T \; 0 \text{ if } I(x,y) < T$$

where *B (x, y)* represents the binary value of the pixel at position (*x, y*).

In this scenario, binarization allows the identification of edges, and detect areas within the image.

2.5 Quantification of Area

For each binarized image, the number of black and white pixels is obtained. Each number 1 in the image matrix is used to determine the number of white pixels, and in order to determine the number of black pixels, the complement of the image is obtained with the equation 2.

Number of black pixels = Total number of pixels - Number of white pixels

Similarly, the area of the pixels is calculated based on the size of the binarized image. This is expressed as presented in equation 3.

Area of white pixels = Number of white pixels × pixel area

Where: *Pixel area* is determined by the physical dimensions of the image and the resolution at which the image was captured.

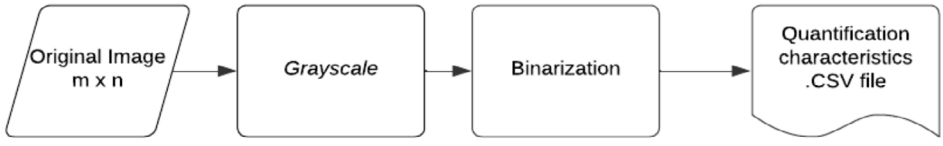

Fig. 1. Flowchart describing the image processing steps and the generated files.

2.6 Edge extraction

In this study, edge extraction was performed using the **Canny edge detection** method, which is widely known for its effectiveness in detecting boundaries while reducing noise. The Canny method involves several key stages to detect edges with high precision. The steps followed for its implementation in Python are outlined as follows:

1. Gaussian Smoothing: A Gaussian filter was applied to smooth the image and reduce noise. This step helps to prevent false edges that may arise due to small variations in pixel intensity. The amount of smoothing is controlled by the kernel size (usually 3x3, 5x5, etc.) and the standard deviation (sigma).

2. Gradient Calculation: The Canny algorithm calculates the gradient magnitude and direction to identify areas of high intensity change. This is done using the Sobel operator, which estimates the first derivatives in both the horizontal and vertical directions (x and y gradients). The gradients represent the rate of change in intensity, which highlights the edges.

3. Non-Maximum Suppression: After the gradient is calculated, non-maximum suppression is applied to thin out the edges, retaining only the most significant ones. This step reduces the number of spurious edges and provides a cleaner result.

4. Edge Tracking by Hysteresis: In this step, two thresholds (high and low) are used to identify strong and weak edges. Strong edges are directly accepted as part of the boundary, while weak edges are only included if they are connected to strong edges. This step ensures that the edges detected are continuous and relevant.

The Canny edge detection was implemented in Python using OpenCV's cv2.Canny() function, which allows for setting the low and high thresholds, as well as other parameters to fine-tune the edge detection process.

2.6.1 Extracted morphological metrics

After edge detection, the contours were extracted from the binary image to measure several morphological properties. These properties provide valuable insights into the shape and structure of the regions of interest. The following metrics were computed:

Average Length (Perimeter): The average length of the contours is the mean perimeter of the detected objects. It can be calculated using the following formula:

$$P = \sum_{i=1}^{n} Length\ of\ countour_i$$

Where: n is the number of contours and length of contour$_i$ is the perimeter of the i-th contour.

Average Area: The area of each contour is calculated using the formula for polygon area. The average area is then obtained by averaging the areas of all contours.

$$A = \sum_{i=1}^{n} Area\ of\ contour_i$$

Where area of contour$_i$ is the area of the i-th contour.

Average Circularity: Circularity measures how close the contour is to a perfect circle. It is calculated using the formula:

$$C = \frac{4\pi A}{P^2}$$

Where A is the area of the contour and P is the perimeter of the contour. A circularity value of 1 indicates a perfect circle.

Average Solidity: Solidity is the ratio of the area of the contour to the area of the convex hull of the contour. It is calculated as:

$$S = \frac{A}{A_{hull}}$$

Where A is the area of the contour, and A$_{hull}$ is the area of the convex hull (the smallest convex shape that encloses the contour).

Average Aspect Ratio: The aspect ratio measures the elongation of the contour and is defined as the ratio of the width to the height of the bounding box that encloses the contour:

$$R = \frac{W}{H}$$

Where W is the width and H is the height of the bounding box.

Number of Contours: The total number of contours detected in the image is simply the count of the contours that were extracted from the binary edge-detected image.

These steps and equations allow to quantify and analyze the morphological properties of the structures detected in the histological images, aiding in a detailed understanding of their characteristics.

2.7 Development of the User Application with Tkinter

For the development of the user application, the Tkinter library is employed. Tkinter is the standard Python interface to the Tk GUI toolkit, and it provides a fast and easy way to create GUI applications. Tkinter is included with the standard Python distribution, making it readily accessible for Python developers.

Tkinter is utilized to design and implement the graphical user interface (GUI) of the application. The following features are integrated into the application using Tkinter:

- **Window Management**: The creation of the main application window and additional dialog boxes for user interaction.

- **Widgets:** The implementation of various widgets such as buttons, labels, text boxes, and menus to facilitate user input and control.

- **Event Handling**: The integration of event-driven programming to handle user actions like button clicks and menu selections, ensuring a responsive user experience.

- **File Handling**: The incorporation of file dialogs to enable users to open, save, and manage image files within the application.

The combination of these features provides a robust and user-friendly interface, allowing users to efficiently process and analyze the acquired images.

2.8 Development Methodology: Iterative and Incremental Approach

The development of the user application follows the Iterative and Incremental approach. This methodology is based on the repetition of a series of iterations to allows a continuous feedback and improvements from the final user. The main steps of this methodology as applied in this proposal is described below:

- **Initial Development**: An initial development of the application is carried on, focusing on the core functions required in the project and for the final user.

- **User Feedback**: The initial version is presented to the end-user, who test the application and provides feedback on its functionality, usability, and any areas needing improvement.

- **Refinement**: Based on the user's feedback, the developers make the necessary changes to improve the application functionality. This includes fixing any issues, adding new features, and improving the user usability.

- **Iteration**: The new and refined version is then presented again to the final user for further feedback. This process is repeated iteratively until the application meets the user's requirements and expectations.

By employing this iterative and incremental approach, the developers ensure that the final application is user-friendly, efficient, and achieve the specific needs of the final user, allowing an early detection and resolution of issues, leading to a more robust and reliable application.

Hematoxylin-eosin staining was performed on slides to identify pneumonic areas, revealing a dose-dependent relationship. The acquired TIFF images were converted to JPEG format using Python version 3.1 and libraries *matplotlib, numpy*, and *cv2* for digital image processing (DIP). The user interface allows selection of folders containing original images for the described process (Figure 2). It also facilitates selection of folders containing binarized images for quantifying black areas (Figure 3).

Fig. 2 Users select the folder containing original images. Results are displayed on-screen upon the process finish.

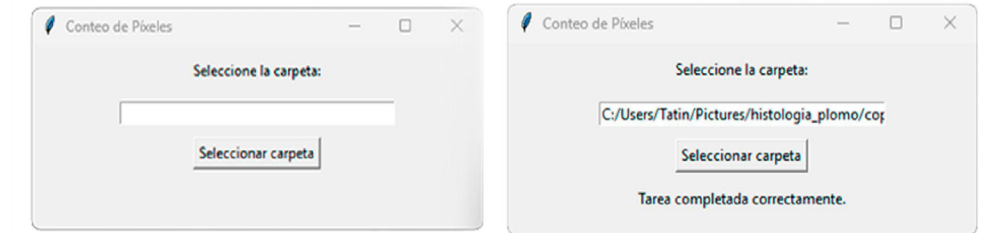

Fig. 3. The interface enables users to select the folder with binarized images. Upon completion, results are displayed on-screen.

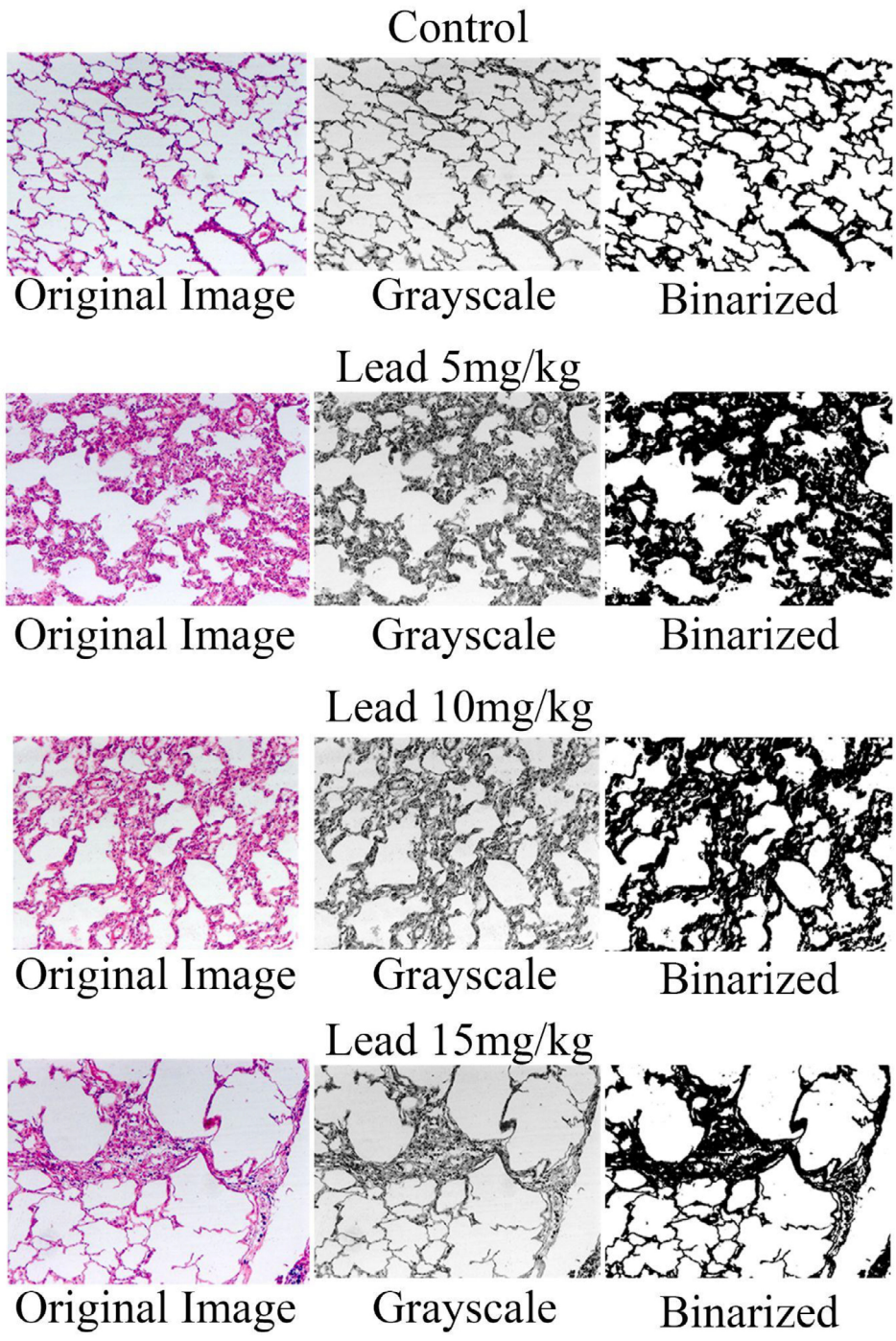

Fig. 4. Comparison of Different Generated Images.

Grayscale conversion applied thresholds (0.2989, 0.5870, 0.1140) producing an image with observable changes for the user. Binarization followed, setting values below the threshold to 0 and above to 255, with thresholds manually adjusted by experts. Representative images are shown in Figure 4 demonstrating the final binarized images stored in JPEG for subsequent area quantification.

The final output is a CSV file containing image file names, counts and areas of black and white pixels. The tests were performed using seven original images with 1384 x 1032 resolution.

The Canny edge detection method was applied to extract the contours of structures in the histological images. The process began with converting the image to grayscale and applying Gaussian smoothing to reduce noise. The gradient magnitude and direction were calculated using the Sobel operator, followed by non-maximum suppression to thin out the edges. Finally, edge tracking by hysteresis was performed to connect weak edges to strong ones, ensuring continuous contours. The extracted contours were then analyzed for various morphological metrics, including average length, area, circularity, solidity, aspect ratio, and the number of contours. The resulting contours provide critical information for understanding the morphological characteristics of the tissue structures, as illustrated in the following image (Figure 5).

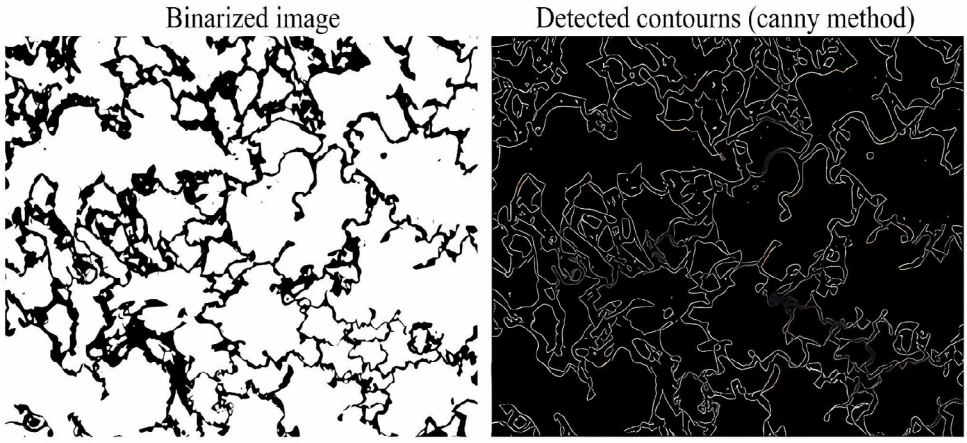

Fig. 5. Binarized histological image (left) and the result of edge detection using the Canny method (right). The binarized image highlights the regions of interest, while the Canny edge detection algorithm effectively identifies the contours of the tissue structures, providing clear boundaries for further morphological analysis.

RESULTS

These results show a statistically significant increase in pneumonic areas in groups treated with lead compared to the negative control group (5mg/kg $p<0.05$, 10mg/kg $p<0.01$, 15mg/kg $p<0.001$) (Table 1). There is also a statistically significant increase ($p<0.05$) in the group treated with 15mg/kg body weight of $Pb(NO_3)_2$ compared to the $NaNO_3$ control group. Also we noted a statistically significant increase in the group of 15mg/kg of body weight of $Pb(NO_3)_2$ compared to the group of 10mg/kg of body weight of $Pb(NO_3)_2$.

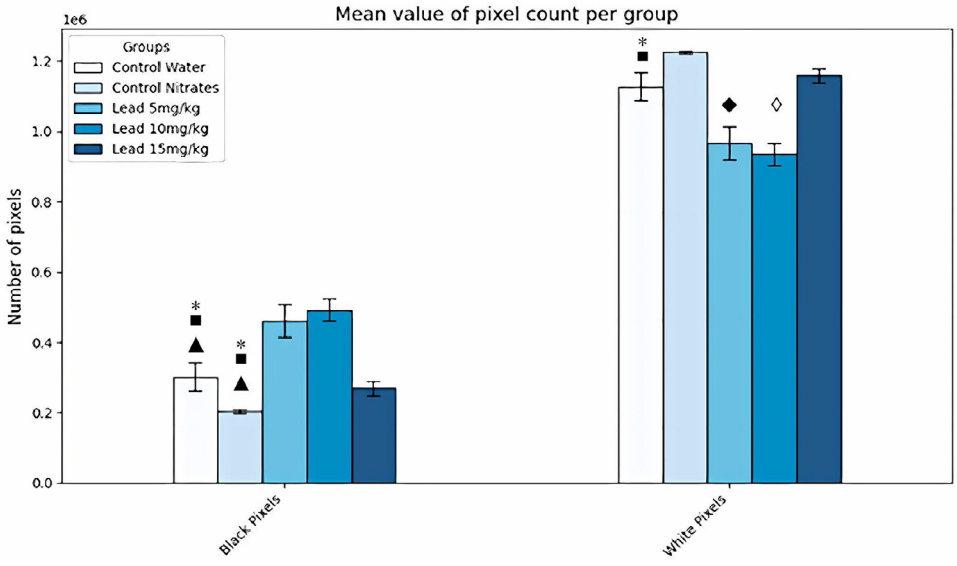

Fig. 6. Bar graphs showing the average pixel count of black pixels (left) and white pixels (right) in the histological images. The graphs illustrate the differences in pixel distribution across the experimental groups and the control group, highlighting variations in tissue characteristics (* Control vs Pb 5 mg/kg, ■ Control vs Pb 10 mg/kg, ▲ Control vs Pb 15mg/kg, ● Pb 5 mg/kg vs Pb 10 mg/kg, ◆Pb 5 mg/kg vs 15 mg/kg and Pb and ◊ 10 mg/kg vs Pb 15 mg/kg).

Table 1. ANOVA results for the different groups regarding the quantity of white pixels and the area of black pixels. Significant differences were observed between the groups, with a p-value < 0.05, indicating statistical significance in both metrics.

Group	Number of black pixels		Area of white pixels %	
	F-Value	P-value	F-Value	P-Value
Control vs Pb 5mg/kg	4.8699	0.0343	4.8699	0.0343
Control vs Pb 10mg/kg	6.2019	0.0179	6.2019	0.0179
Control vs Pb 15mg/kg	13.6331	0.0008	20.3207	0.8254
Pb 5mg/kg vs Pb 10mg/kg	0.022	0.8827	0.022	0.8827
Pb 5mg/kg vs Pb 15mg/kg	1.3484	0.2538	2.9639	0.0945
Pb 10mg/kg vs Pb 15mg/kg	2.094	0.1573	4.352	0.0447

The analysis of morphological features revealed significant differences between the experimental groups ($p < 0.05$) see (Table 2, Table 3, Table 4). These differences can be attributed to alterations induced by apoptotic processes, inflammation, and fibrosis. The observed variations in tissue structure align with the pathological changes associated with these cellular processes, suggesting that exposure to lead may activate mechanisms that disrupt cellular homeostasis and promote tissue damage.

Table 2. ANOVA results for the different groups comparing the average lengths and areas of extracted edges. Significant differences were observed between the control group and the treatment groups, with a p-value < 0.05, indicating statistical significance in edge length.

Group	Average Lengths		Average Areas	
	F-Statistic	P-Value	F-Statistic	P-Value
Control vs Pb 5mg/kg	13.4176713	0.00436726	3.27563009	0.10042356
Control vs Pb 10mg/kg	6.69537332	0.04134823	1.5344996	0.26169976
Control vs Pb 15mg/kg	4.47763601	0.08794557	1.9383782	0.22259372
Pb 5mg/kg vs Pb 10mg/kg	0.19417777	0.67112661	0.01499496	0.90555984
Pb 5mg/kg vs Pb 15mg/kg	0.24905295	0.63304162	0.53388689	0.48870582
Pb 10mg/kg vs Pb 15mg/kg	0.05868566	0.82420211	5.73658097	0.09629668

Although significant differences are observed in the average length metric between the groups, it is interesting to note that there are no significant differences between groups with different lead concentrations, such as Pb 5 mg/kg, compared to the other experimental groups, Pb 10 mg/kg and Pb 15 mg/kg. However, a significant difference is observed between the control group and the Pb 5 mg/kg and Pb 10 mg/kg groups. Additionally, regarding the analyzed average area metric, no significant differences are observed between any of the groups (table 2).

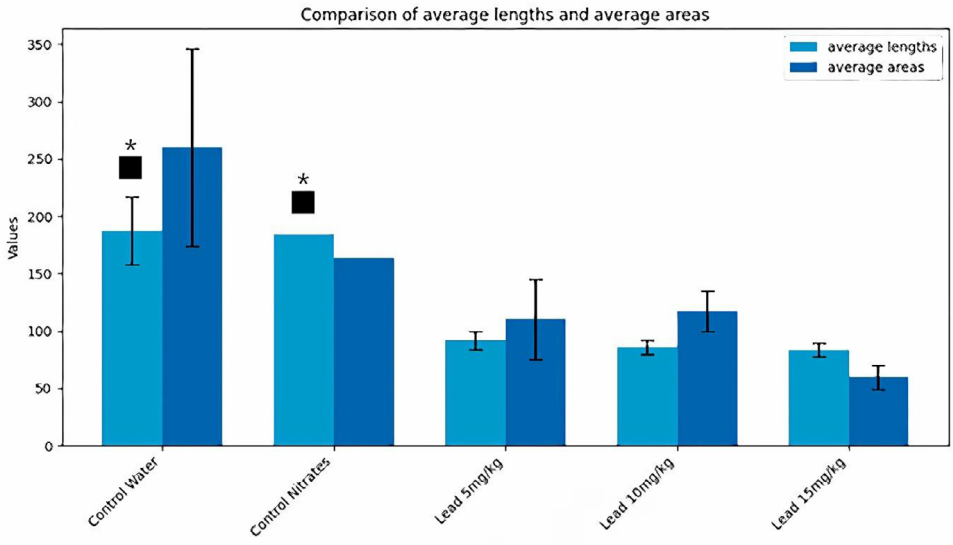

Fig. 7. Bar graphs depicting the average lengths and areas of the detected edges in the histological images. The graphs highlight differences in pixel distribution between the experimental groups and the control group, emphasizing variations in tissue characteristics (* Control vs Pb 5 mg/kg, ■ Control vs Pb 10 mg/kg, ▲ Control vs Pb 15 mg/kg, ● Pb 5 mg/kg vs Pb 10 mg/kg, ◆ Pb 5 mg/kg vs 15 mg/kg and Pb and ◊ 10 mg/kg vs Pb 15 mg/kg).

Table 3. ANOVA results for the different groups comparing the average circularity and solidity of extracted edges. Significant differences were observed between the control group and the treatment groups, with a p-value < 0.05, indicating statistical significance in both metrics.

Group	Average circularities		Average Solidity	
	F-Statistic	P-Value	F-Statistic	P-Value
Control vs Pb 5mg/kg	15.7160415	0.00266762	19.4320763	0.00131815
Control vs Pb 10mg/kg	45.4321066	0.00051949	46.9040987	0.00047669
Control vs Pb 15mg/kg	4.49078845	0.08760011	7.9278519	0.03729941
Pb 5mg/kg vs Pb10mg/kg	1.20E-06	0.99915429	0.05529784	0.81999604
Pb 5mg/kg vs Pb15mg/kg	2.49573621	0.15816577	1.96059705	0.20417988
Pb 10mg/kg vs Pb 15mg/kg	108.037305	0.00190031	42.4591114	0.00734285

Moreover, regarding the average circularity metric, significant differences are observed in the comparisons between the control group and the Pb 5 mg/kg and Pb 10 mg/kg groups, as well as between the Pb 10 mg/kg and Pb 15 mg/kg groups. No significant differences are observed in the remaining comparisons. Meanwhile, in the average solidity metric, significant differences are observed between the control group and the Pb 5 mg/kg, Pb 10 mg/kg and Pb 15 mg/kg groups, and between the Pb 10 mg/kg and Pb 15 mg/kg groups (Table 3).

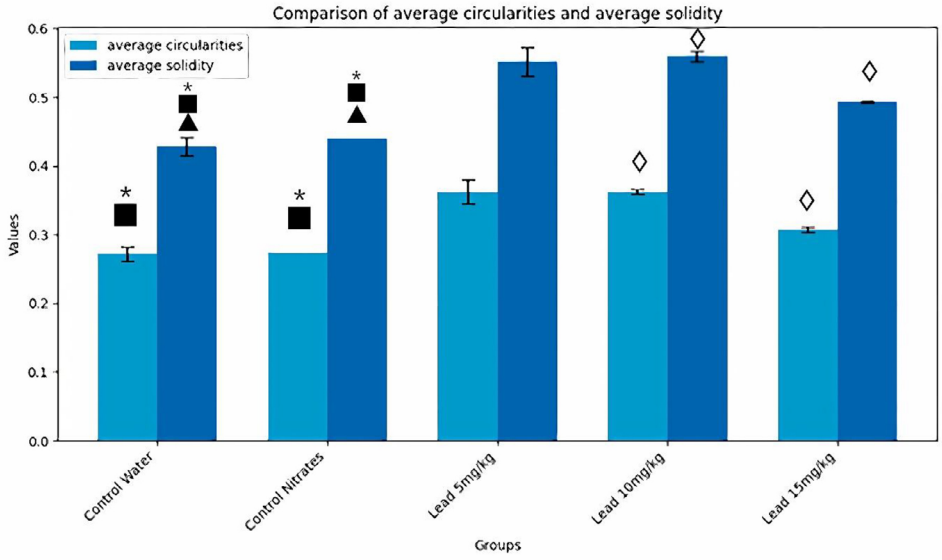

Fig. 8. Bar graphs showing the average circularity and solidity of the analyzed tissues. Significant differences were observed in both morphological characteristics across the groups (* Control vs Pb 5 mg/kg, ■ Control vs Pb 10 mg/kg, ▲ Control vs Pb 15 mg/kg, ● Pb 5 mg/kg vs Pb 10 mg/kg, ◆ Pb 5 mg/kg vs 15 mg/kg and Pb and ◊ 10 mg/kg vs Pb 15mg/kg).

Table 4. ANOVA results for the diverse groups comparing the average aspect ratio and number of contours of extracted edges. Significant differences were observed between the control group and the treatment groups, with a p-value < 0.05, indicating statistical significance in both metrics.

Group	Average circularities		Average Solidity	
	F-Statistic	P-Value	F-Statistic	P-Value
Control vs Pb 5mg/kg	15.7160415	0.00266762	19.4320763	0.00131815
Control vs Pb 10mg/kg	45.4321066	0.00051949	46.9040987	0.00047669
Control vs Pb 15mg/kg	4.49078845	0.08760011	7.9278519	0.03729941
Pb 5mg/kg vs Pb10mg/kg	1.20E-06	0.99915429	0.05529784	0.81999604
Pb 5mg/kg vs Pb15mg/kg	2.49573621	0.15816577	1.96059705	0.20417988
Pb 10mg/kg vs Pb 15mg/kg	108.037305	0.00190031	42.4591114	0.00734285

The values obtained in the comparisons of the aspect ratio metric show significant differences between the control group and the Pb 5 mg/kg and Pb 10 mg/kg groups. Additionally, significant differences are observed among the experimental groups, specifically between Pb 5 mg/kg vs. Pb 10 mg/kg and Pb 10 mg/kg vs. Pb 15 mg/kg. Meanwhile, in the average number of contours metric, significant differences are observed only in the comparisons between the control group and the Pb 10 mg/kg and Pb 15 mg/kg groups. (Table 4).

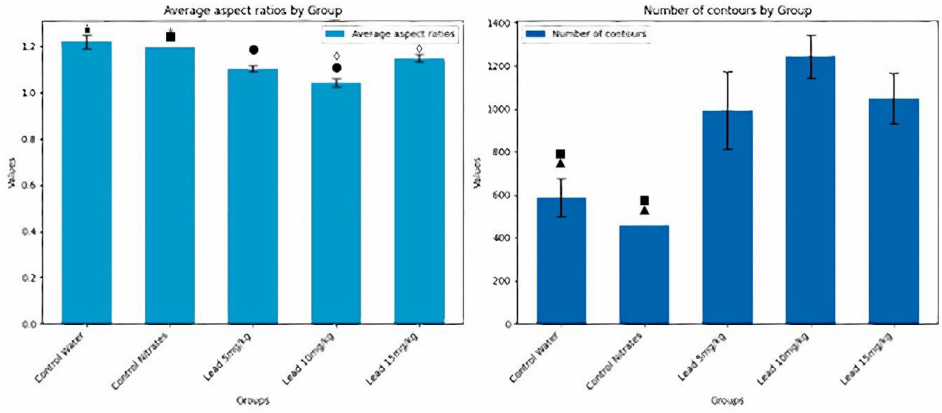

Fig. 9. On the left, bar graphs display comparisons between the groups for the "aspect ratio" metric, on the right, the graphs show the number of detected contours. Significant differences are evident in both metrics, with the control group differing notably from the experimental groups (* Control vs Pb 5 mg/kg, ■ Control vs Pb 10mg/kg, ▲ Control vs Pb 15 mg/kg, ● Pb 5 mg/kg vs Pb 10 mg/kg,◆ Pb 5 mg/kg vs 15 mg/kg and Pb and ◊ 10 mg/kg vs Pb 15 mg/kg).

DISCUSSIONS AND CONCLUSIONS

The results show lung damage on the lead treated individuals. When these images were processed in the software created by Gerardo Neftalí Rivera Rojas from the Master's Degree in Information Processing Sciences at the Autonomous University of Zacatecas, a statistically significant increase in pneumonic areas was observed in male Wistar rats treated with lead nitrate at doses of 5 mg/kg, 10 mg/kg, and 15 mg/kg compared to the control group (Figure 4). Additionally, previous studies on Wistar rats exposed to approximately 500 mg/L per day for one and two weeks reported an increased number of lymphocytes in the treated groups compared to controls, further highlighting the immune response to lead exposure (Adeyomoye & Adewumi, 2019). The increase in lymphocytes may be associated with pro-inflammatory processes, linked to the thickening of the alveolar tissue.

Some structural alterations were found in these images, including disorganization of the alveoli and thickened interalveolar septa. These findings may indicate that the lung tissue had undergone fibrosis, which coincides with our results (ONARLIOĞLU et al., 1999). In Masson's trichome stain you can see black nuclei, reddish muscle and cytoplasm, and blue or green collagen, responsible for maintaining the adequate elasticity that allows the lung to carry out its mechanical activity, therefore, when these fibers disappear, it indicates a process of pulmonary fibrosis (Carrera &

Hernan, 2013). Image processing and basic quantification of alveolar tissue allow inference of potential morphological changes, aiding professionals in assessing structural damage.

This study addresses morphological characteristics that may be associated with lung tissue damage due to chronic lead exposure in Wistar rats. Metrics such as tissue area, contour count, solidity, length, aspect ratio, and circularity could serve as quantifiable indicators of damage, not only through the increase in alveolar tissue thickness. This initial approach paves the way for the quantifiable analysis of lung damage using microscopic images. These processes, taking a few minutes on many current devices, could benefit scientists involved in this specific research. Additionally, quantification of regions of interest such as nuclei, collagen accumulations, or texture differences features reported by (Ségard et al., 2024) will be considered for future improvements to the software presented.

Ethical statement

The project was approved by the Research Committee (COFEPRIS-19CI 32056045) and the Bioethics Committee (CEI-UAO/UAZ0002-R/2022).

REFERENCES

Adeyomoye, O. I., & Adewumi, N. A. (2019). Lead exposure causes alteration of haematological indices in adult female Wistar rats. *Asian Journal of Pharmaceutical Research and Development*, *7*(6), 30-34.

Aschner, M., Skalny, A. V., Lu, R., Santamaria, A., Zhou, J.-C., Ke, T., Karganov, M. Y., Tsatsakis, A., Golokhvast, K. S., & Bowman, A. B. (2023). The role of hypoxia-inducible factor 1 alpha (HIF-1α) modulation in heavy metal toxicity. *Archives of Toxicology*, *97*(5), 1299-1318.

Carrera, L. G., & Hernan, G. B. (2013). Pulmonary manifestations of collagen diseases. *Archivos de Bronconeumología (English Edition)*, *49*(6), 249-260.

Charkiewicz, A. E., & Backstrand, J. R. (2020). Lead Toxicity and Pollution in Poland. *International Journal of Environmental Research and Public Health*, *17*(12). https://doi.org/10.3390/ijerph17124385

Dietert, R. R., & Piepenbrink, M. S. (2006). Lead and immune function. *Critical reviews in toxicology*, *36*(4), 359-385.

Ding, X., He, R., Zhang, T., Mei, L., Zhu, S., Wang, C., Liao, Y., Wang, D., Wang, H., & Guo, J. (2023). Lung toxicity and molecular mechanisms of lead-based perovskite nanoparticles in the respiratory system. *ACS Applied Materials & Interfaces*, *15*(36), 42139-42152.

Dos Santos, N. R., Rodrigues, J. L. G., Bandeira, M. de J., Anjos, A. L. dos S., Araújo, C. F. da S., Adan, L. F. F., & Menezes-Filho, J. A. (2022). Manganese and lead exposure and early puberty onset in children living near a ferromanganese alloy plant. *International journal of environmental research and public health*, *19*(12), 7158.

Fang, Y., Lu, L., Liang, Y., Peng, D., Aschner, M., & Jiang, Y. (2021). Signal transduction associated with lead-induced neurological disorders: A review. *Food and Chemical Toxicology*, *150*, 112063.

Hoover, C., Dickerson, A. S., Specht, A. J., & Hoover, G. G. (2023). Firearm-related lead exposure and pediatric lead levels in Massachusetts: A decade of evidence (2010-2019). *Environmental Research*, *227*, 115719. https://doi.org/10.1016/j.envres.2023.115719

Hübner, R.-H., Gitter, W., Eddine El Mokhtari, N., Mathiak, M., Both, M., Bolte, H., Freitag-Wolf, S., & Bewig, B. (2008). Standardized quantification of pulmonary fibrosis in histological samples. *Biotechniques*, *44*(4), 507-517.

Jiang, C.-B., Kao, C.-S., Chien, L.-C., Chen, Y.-J., & Liao, K.-W. (2022). Associations among prenatal and postnatal arsenic, lead, and cadmium exposures and motor development in 3-year-old children: A longitudinal birth cohort study in Taiwan. *Environmental Science and Pollution Research*, *29*(28), 43191-43200.

Jing, H., Zhang, Q., Li, S., & Gao, X. (2020). Pb exposure triggers MAPK-dependent inflammation by activating oxidative stress and miRNA-155 expression in carp head kidney. *Fish & Shellfish Immunology*, *106*, 219-227.

Kothapalli, C. R. (2021). Differential impact of heavy metals on neurotoxicity during development and in aging central nervous system. *Current Opinion in Toxicology*, *26*, 33-38.

Kou, H., Ya, J., Gao, X., & Zhao, H. (2020). The effects of chronic lead exposure on the liver of female Japanese quail (Coturnix japonica): Histopathological damages, oxidative stress and AMP-activated protein kinase based lipid metabolism disorder. *Ecotoxicology and environmental safety*, *190*, 110055.

Kumar, A., Kumar, A., MMS, C.-P., Chaturvedi, A. K., Shabnam, A. A., Subrahmanyam, G., Mondal, R., Gupta, D. K., Malyan, S. K., & Kumar, S. S. (2020). Lead toxicity: Health hazards, influence on food chain, and sustainable remediation approaches. *International journal of environmental research and public health*, *17*(7), 2179.

Lee, H. J., & Lee, H.-Y. (2024). Characterization of lung function impairment and pathological changes induced by chronic lead and cadmium inhalation: Insights from a mouse model study. *Ecotoxicology and Environmental Safety*, *283*, 116776.

Li, L., Li, W., Liu, Y., Jin, X., Yu, Y., & Lin, H. (2023). TBBPA and lead co-exposure induces grass carp liver cells apoptosis via ROS/JAK2/STAT3 signaling axis. *Fish & Shellfish Immunology*, *142*, 109100.

ONARLIOĞLU, B., ONARLIOĞLU, T., & Erdal, S. (1999). The Effect of Lead Inhalation on Rat LungMorphology. *Turkish Journal of Medical Sciences*, *29*(6), 617-622.

Paithankar, J. G., Saini, S., Dwivedi, S., Sharma, A., & Chowdhuri, D. K. (2021). Heavy metal associated health hazards: An interplay of oxidative stress and signal transduction. *Chemosphere*, *262*, 128350.

Ségard, B.-D., Kimura, K., Matsuoka, Y., Imamura, T., Ikeda, A., & Iwamiya, T. (2024). Quantification of fibrosis extend and airspace availability in lung: A semi-automatic ImageJ/Fiji toolbox. *Plos one*, *19*(2), e0298015.

Tarragó, O., & Brown, M. J. (2017). *Lead toxicity*.

Wang, D., Fu, X., Zhang, J., Xu, C., Hu, Q., & Lin, W. (2020). Association between blood lead level during pregnancy and birth weight: A meta-analysis. *American Journal of Industrial Medicine*, *63*(12), 1085-1094.

Wang, L., Zheng, Y., Zhang, G., Han, X., Li, S., & Zhao, H. (2021). Lead exposure induced inflammation in bursa of Fabricius of Japanese quail (C. japonica) via NF-κB pathway activation and Wnt/β-catenin signaling inhibition. *Journal of Inorganic Biochemistry*, *224*, 111587.

Wang, X., Mukherjee, B., & Park, S. K. (2018a). Associations of cumulative exposure to heavy metal mixtures with obesity and its comorbidities among US adults in NHANES 2003–2014. *Environment international*, *121*, 683-694.

Wang, X., Mukherjee, B., & Park, S. K. (2018b). Associations of cumulative exposure to heavy metal mixtures with obesity and its comorbidities among US adults in NHANES 2003–2014. *Environment international*, *121*, 683-694.

West, C. M., Ivy, C. M., Husnudinov, R., & Scott, G. R. (2021). Evolution and developmental plasticity of lung structure in high-altitude deer mice. *Journal of Comparative Physiology B*, *191*, 385-396.

Xu, L., Huo, X., Liu, Y., Zhang, Y., Qin, Q., & Xu, X. (2020). Hearing loss risk and DNA methylation signatures in preschool children following lead and cadmium exposure from an electronic waste recycling area. *Chemosphere*, *246*, 125829.

Yu, Y.-L., Yang, W.-Y., Hara, A., Asayama, K., Roels, H. A., Nawrot, T. S., & Staessen, J. A. (2023). Public and occupational health risks related to lead exposure updated according to present-day blood lead levels. *Hypertension Research: Official Journal of the Japanese Society of Hypertension*, *46*(2), 395-407. https://doi.org/10.1038/s41440-022-01069-x

Further considerations:

The authors believe that a larger sample of subjects would be helpful for improving the sensitivity of results.